Bulletin of the Seismological Society of America, Vol. 94, No. 6, pp. 2064–2078, December 2004

# Near-Source Ground Motions from Simulations of Sustained Intersonic and Supersonic Fault Ruptures

by Brad T. Aagaard and Thomas H. Heaton

Abstract We examine the long-period near-source ground motions from simulations of *M* 7.4 events on a strike-slip fault using kinematic ruptures with rupture speeds that range from subshear speeds through intersonic speeds to supersonic speeds. The strong along-strike shear-wave directivity present in scenarios with subshear rupture speeds disappears in the scenarios with ruptures propagating faster than the shear-wave speed. Furthermore, the maximum horizontal displacements and velocities rotate from generally fault-perpendicular orientations at subshear rupture speeds to generally fault-parallel orientations at supersonic rupture speeds. For rupture speeds just above the shear-wave speed, the orientations are spatially heterogeneous as a result of the random nature of our assumed slip model. At locations within a few kilometers of the rupture, the time histories of the polarization of the horizontal motion provide a better diagnostic with which to gauge the rupture speed than the orientation of the peak motion. Subshear ruptures are associated with significant fault-perpendicular motion *before* fault-parallel motion close to the fault; supershear ruptures are associated with fault-perpendicular motion *after* significant fault-parallel motion. Consistent with previous studies, we do not find evidence for prolonged supershear rupture in the long-period (>2 sec) ground motions from the 1979 Imperial Valley earthquake. However, we are unable to resolve the issue of whether a limited portion of the rupture (approximately 10 km in length) propagated faster than the shear-wave speed. Additionally, a recording from the 2002 Denali fault earthquake does appear to be qualitatively consistent with locally supershear rupture. Stronger evidence for supershear rupture in earthquakes may require very dense station coverage in order to capture these potentially distinguishing traits.

## Introduction

Observations of crustal earthquakes indicate that fault ruptures tend to propagate at around 80% of the shear-wave speed (e.g., Heaton, 1990), which is a little below the theoretically limiting speed. On some occasions the ruptures appear to propagate at a speed that exceeds the shear-wave speed. Two well-studied cases of plausible supershear rupture include the 1979 Imperial Valley, California, earthquake (Olson and Apsel, 1982; Archuleta, 1984; Spudich and Cranswick, 1984) and the 1999 Kocaeli (Izmit), Turkey, earthquake (Anderson, 2000; Bouchon *et al.*, 2000, 2001; Sekiguchi and Iwata, 2002; Thio *et al.*, 2004), although there is still much debate about the robustness of the conclusions that the rupture speeds were supershear for these cases (Hartzell and Heaton, 1983; Archuleta, 1984; Thio *et al.*, 2004). Other possible cases of supershear rupture include the 2001 Kunlunshan, Tibet, earthquake (Bouchon and Vallee, 2003) and the 2002 Denali fault, Alaska, earthquake (Dunham and Archuleta, 2004; Ellsworth *et al.*, 2004).

Olson and Apsel (1982) inferred that the rupture in the 1979 Imperial Valley earthquake propagated faster the shear-wave speed from their source inversion. However, Hartzell and Heaton (1983) argued that the waveforms could be simulated with a rupture speed that varied between 70% and 90% of the shear-wave speed, and that the estimate of supershear rupture by Olson and Apsel was the result of excessive smoothing of the distribution of slip in the inversion. Archuleta (1984) maintained that trial and error matching of the waveforms with a zone of supershear rupture similar to the one proposed by Olson and Apsel created a better fit than the one obtained by Hartzell and Heaton. Additionally, Spudich and Cranswick (1984) examined the data from the 213-m El Centro differential array and found evidence in the high-frequency (>1.5 Hz) motion consistent with supershear propagation of the leading edge of the rupture, although the location of the supershear rupture lies slightly north of the region suggested by Archuleta.

In the 1999 Kocaeli earthquake, Bouchon *et al.* (2001) found that the shear-wave arrival for the Sakarya (SKR) re-

cording is consistent with 50 km of supershear rupture. Digital records of fault-parallel (east–west) and vertical accelerations were obtained at Sakarya about 1 km north of the fault rupture and 40 km east of the epicenter. Unfortunately, this station did not have a synchronized clock. Furthermore, the fault-perpendicular (north–south) component malfunctioned. Second time integrals of the SKR records show a fault-parallel displacement that is dominated by a 5-sec linear ramp, which Bouchon *et al.* interpreted as the near-field shear wave radiated from the fault adjacent to the station. A key feature of the SKR displacement record is that the displacements are very small prior to the onset of the ramp. Bouchon *et al.* simulated the SKR displacements with a supershear rupture speed that produces near-nodal dilatational waves and very short *S-P* times. However, Bouchon *et al.*'s simulated dilatational-wave displacements are much larger than those in the SKR record. If their interpretation is correct, then SKR experiences near-nodal dilatational waves even smaller than those produced along the strike of vertical strike-slip fault in a layered half-space model. Alternatively, Thio *et al.* (2004) favor onset of rupture on the Sakarya segment from triggering by the arrival of the dilatational wave, not supershear rupture on the Sapanca Lake segment. Nevertheless, if the the SKR record is correct, then there is strong support for at least a supershear *apparent* rupture speed.

Arguably stronger evidence for supershear rupture comes from the 2002 Denali fault earthquake. In this event all three components were successfully recorded within a few kilometers of the fault at pump station 10 along the Alyeska pipeline. As we will discuss in detail later, the polarization of the motion is consistent with supershear rupture. Finally, through kinematic forward modeling of the 2001 Kunlunshan earthquake, Bouchon and Vallee (2003) concluded that regional surface wave observations were best fit with supershear rupture over several hundred kilometers.

Whereas these earthquake case histories generally provide only circumstantial evidence for the existence of supershear rupture in earthquakes, laboratory experiments with propagating mode-II cracks and numerical models of earthquake ruptures actually corroborate the existence of ruptures that propagate at supershear speeds. Experiments by Rosakis *et al.* (1999) and Xia *et al.* (2004) demonstrated that shear cracks could propagate at intersonic speeds in homalite (a brittle polyester resin) from either projectile impact loading or shear loading with nucleation controlled by an exploding wire. Analytical models of steady-state rupture demonstrate that mode-II shear cracks can indeed propagate stably at this speed (Freund, 1979; Broberg, 1994, 1995; Samudrala *et al.*, 2002). Numerical simulations of dynamic earthquake ruptures support extrapolation of these laboratory findings to earthquake ruptures (Burridge, 1973; Andrews, 1976; Das and Aki, 1977; Das, 1981, Day, 1982). For example, Andrews (1976) demonstrated that mode-II shear cracks could accelerate from subshear rupture speeds to the Eshelby speed. More recently, Madariaga and Olsen (2000) established that the ratio of the the energy release rate to the fracture energy controls the speed of propagation in these numerical models, with higher values allowing supershear rupture speeds. Aagaard *et al.* (2001) found large slip rates near the free surface combined with a high apparent rupture speed along the surface enabled ruptures to propagate stably near the Eshelby speed.

The four cases of suspected supershear rupture in real earthquakes mentioned earlier occur on strike-slip faults. While it is clear that a rupture propagating at slightly below the shear-wave speed for this geometry creates strong directivity in the shear wave radiated along the strike of the fault, what happens to the ground motions when the rupture accelerates to faster speeds? Does the mechanism for directivity break down? How do the characteristics of the ground motions change? We investigate these issues by computing the long-period near-source ground motions using kinematic ruptures by forcing the rupture to propagate at a given rupture speed. We examine the characteristics of the ground motions and look for features that undergo significant changes as the scenarios vary over a wide range of rupture speeds. We then use these features to examine records from the Imperial Valley and Denali fault earthquakes to see if the evidence supports supershear rupture.

## Methodology

We employ the finite-element method to solve the three-dimensional dynamic elasticity equation with a kinematic source. We select a kinematic source because we want to examine the effect of rupture speed on the near-source ground motions for a continuous range of rupture speeds from subshear speeds to supersonic speeds. While a dynamic (spontaneous) rupture source can generate more physically realistic ruptures (assuming the constitutive relations governing the fault rupture are chosen correctly), the rupture speeds are restricted only to those allowed by the assumed fault constitutive relations; the rupture speed depends on the ratio of the strain energy release rate to the fracture energy associated with the friction model (Day, 1982; Madariaga and Olsen, 2000). On the other hand, these dynamic rupture models do allow behavior not present in most kinematic source models, such as bifurcation of the rupture into supershear and subshear slip pulses (see, e.g., Aagaard *et al.*, 2001 and Dunham and Archuleta, 2004). This means that by choosing to use kinematic sources for ruptures propagating at various speeds with only a single slip pulse, we are focusing on the seismic radiation from the leading edge of the rupture.

These simulations follow the same methodology and use the finite-element model from our previous work that examined the effect of fault geometry on near-source ground motions (Aagaard *et al.*, 2004). The length scale of the discretization allows accurate propagation of waves with periods of 2 sec and longer. The domain encompasses a region 160 km long, 80 km wide, and 40 km deep, as shown in Figure 1. We focus on the results from a layered half-space

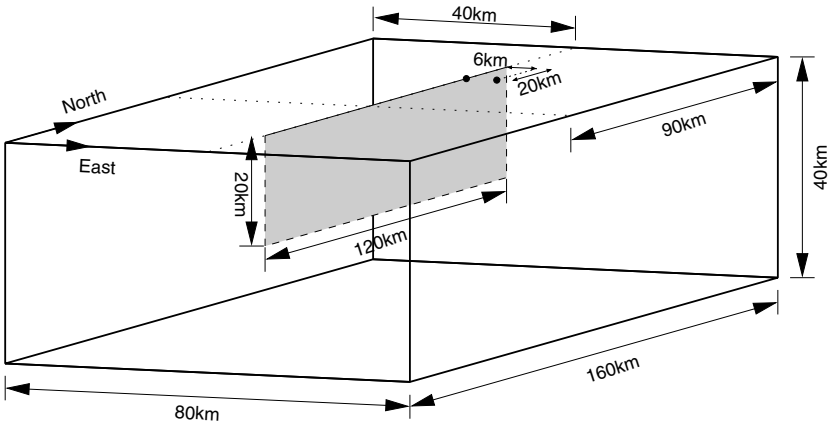


Figure 1. Geometry of the simulation domain. The center of the fault lies 10 km south of the center of the domain. We examine shear-wave polarization at the sites denoted by the dots, which sit at distances of 0 km and 6 km from the fault trace near the northern end of the rupture.

with a spatially heterogeneous slip distribution, but we also refer to results from a uniform half-space with spatially uniform slip to highlight the principal observations. Figure 2 and Table 1 display the variation in the material properties as a function of depth for the layered half-space. For the uniform half-space we use the material properties from a depth of 90 km in the layered half-space.

The kinematic source uses the integral of Brune's far-field time function,

$$\frac{D(x,y,z,t)}{D_\infty(x,y,z)} = 1-\exp\left(\frac{-(t-t_0(x,y,z))}{\tau(x,y,z)}\right)\left(1+\frac{t-t_0(x,y,z)}{\tau(x,y,z)}\right) \quad (1)$$

$$\tau(x,y,z) = \frac{D_\infty(x,y,z)}{\dot{D}_{\max} e},$$

for the slip time history with the final slip ($D_\infty$ ($x$,$y$,$z$)), peak slip rate ($\dot{D}_{\max}$), and slip starting time ($t_0$ ($x$,$y$,$z$)) as parameters. For the layered half-space with spatially heterogeneous slip, as shown in Figure 3, we low-pass filter a uniform random distribution using a first-order (single-pole, causal) Butterworth filter. The average slip is 2.9 m with a maximum value of 7.1 m, which results in events with a moment magnitude of 7.4. For the uniform half-space the slip is 2.9 m over the entire fault. In both sets of simulations, we use a uniform peak slip rate of 2.0 m/sec. With spatially heterogeneous slip, this creates variations in the slip duration.

The hypocenter lies approximately middepth one-quarter of the distance along the strike of the fault. Figure 4 displays the relative location of the hypocenter as well as the propagation of the rupture using an anisotropic specification of the rupture speed. By using kinematic ruptures, we can force the ruptures to propagate at any given speed, including those that would be unstable for dynamic shear cracks. The relative rupture speed in the mode-II and mode-III directions depends on the fracture energy, with the speed in the mode-III (perpendicular to slip) direction more sensitive to the level of fracture energy compared with the mode-II (parallel to slip) direction (Andrews, 1976; Day, 1982; Freund, 1990; Madariaga *et al.*, 1998). This means that faster rupture speeds in our kinematic ruptures correspond to smaller fracture energies. With mode-III rupture more sensitive to the fracture energy than mode-II rupture, the ratio of the mode-II to mode-III rupture speed generally increases with faster rupture speeds. The precise nature of this relationship between the relative rupture speeds, however, has yet to be determined. For this reason, we choose a mode-III rupture speed that is 20% slower than the mode-II rupture speed, which is consistent with the relative speeds generally observed in numerical models of subshear rupture. Although this results in mode-III rupture speeds that exceed the shear-wave speed (which is theoretically impossible) in the cases where the mode-II rupture speeds exceeds 1.25 times the shear-wave speed, this is not a significant issue because the earthquakes are dominated by mode-II rupture. Table 2 gives the rupture speeds for each simulation. The infinite rupture speed corresponds to simultaneous rupture of the entire fault. Thus, the only variation in the kinematic source in each suite of models (uniform half-space and layered half-space) is the change in rupture speed; the slip time

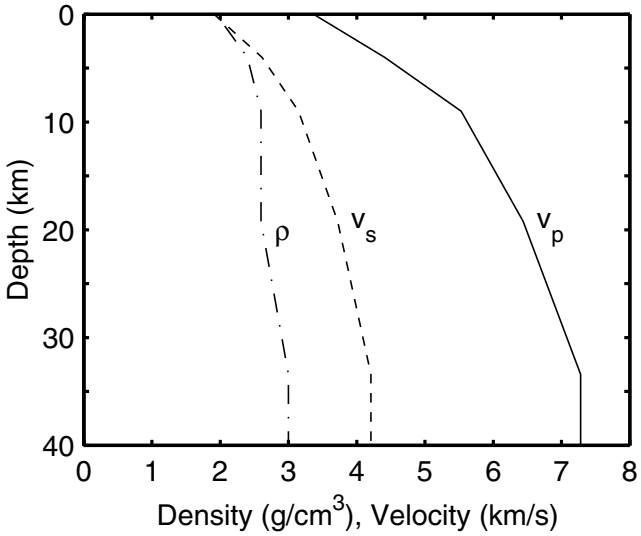


Figure 2. Dilatational-wave speed ($v_p$), shear-wave speed ($v_s$), and mass density ($\rho$) as a function of depth for the layered half-space.

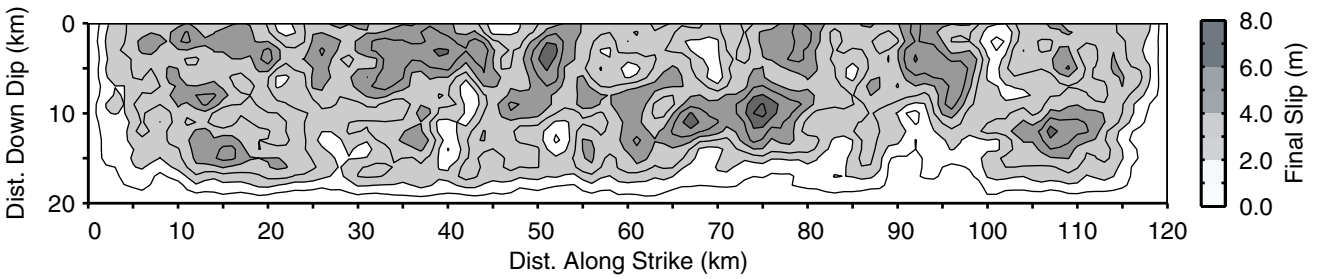


Figure 3. Distribution of final slip created from low-pass filtering a random distribution. The average slip is 2.9 m, with a maximum value of 7.1 m, yielding a moment magnitude of 7.4.

Table 1
Control Points Describing Linear Variation of Material Properties with Depth in the Layered Half-Space

| Depth (km) | Mass Density (kg/m$^3$) | Dilatational-Wave Speed (km/sec) | Shear-Wave Speed (km/sec) |
|---|---|---|---|
| 0 | 1943 | 3.37 | 1.91 |
| 4.0 | 2400 | 4.41 | 2.62 |
| 9.0 | 2600 | 5.53 | 3.15 |
| 19.2 | 2600 | 6.44 | 3.72 |
| 33.4 | 3000 | 7.28 | 4.21 |
| 40.0 | 3000 | 7.28 | 4.21 |

histories are kept constant at each point on the fault except for the time at which slip begins, corresponding to changes in the rupture speed.

## Results

We begin our analysis of how increasing the rupture propagation speed from subshear speeds through intersonic speeds to supersonic speeds affects near-source ground motions by examining the snapshots of the particle velocities on the ground surface for six of the rupture speeds. Two ruptures fall into each of the three regimes (subshear, intersonic, and supersonic). The snapshots for both the uniform half-space and layered half-space display very similar trends, so we show only the ground velocities for the layered half-space. Figure 5 displays the fault-perpendicular and fault-parallel components of the velocity of the ground surface after the rupture has propagated about 65 km down the length of the fault for each of the six scenarios.

The two ruptures that propagate at or below the shear-wave speed in the mode-II direction generate significant shear-wave rupture directivity by reinforcing the far-field shear wave radiated along the strike of the fault (see Somerville *et al.* [1997] for a thorough discussion). This far-field shear wave, which has particle motion perpendicular to the fault and was generated by slip at locations earlier in the rupture, arrives before the near-field shear wave, which has particle motion parallel to the fault and was generated by slip at locations nearby. Thus, a site close to the surface rupture undergoes large-amplitude fault-perpendicular motion *prior* to fault-parallel motion. With the horizontally layered medium, these shear waves with fault-perpendicular particle motion develop into large-amplitude Love waves. The anisotropic rupture speed and the depth-dependent structure diminish the sharpness of the abrupt shear-wave arrival for rupture at the shear wave speed, so the maximum particle velocities do not approach extremely large values (relative to the theoretical limit of infinite velocities in continuum models of ruptures propagating in the mode-II direction precisely at the shear-wave speed).

As the rupture speed increases into the intersonic range, the sharp arrival of this shear wave forms a Mach cone emanating from the leading edge of the rupture. The rupture propagates faster than the shear-wave speed so that at locations near the fault trace, the shear wave radiated along the strike of the fault (from locations earlier in the rupture) arrives after the shear wave radiated perpendicular to the fault (from locations nearby). Consequently, a site near the surface trace of supershear rupture experiences its large-amplitude fault-perpendicular motion *after* fault-parallel motion. Additionally, the directivity-induced reinforcement of the far-field shear wave propagating along the strike of the fault decreases substantially. This leads to a decrease in the amplitude of motion in the fault-perpendicular component. Meanwhile, with nearby areas of the fault rupturing within a shorter time window, the shear wave radiated perpendicular to the fault begins to grow in amplitude. This process continues as the rupture speed moves into the supersonic regime. For an infinite rupture speed (simultaneous rupture of the entire fault), this shear wave radiated perpendicular to the fault (as opposed to the shear wave radiated along the strike of the fault) dominates the near-source motion. We examine the variation in the polarization of the shear wave at several sites as a function of the shear-wave speed in more detail later.

We now turn to the maximum horizontal displacements and maximum peak-to-peak velocities displayed in Figure 6 to show how the spatial distribution of the shaking changes with rupture speed. We determine the maximum peak-to-peak velocity by finding the maximum amplitude between consecutive peaks in the velocity time histories after resolving the horizontal velocity into all possible horizontal ori-

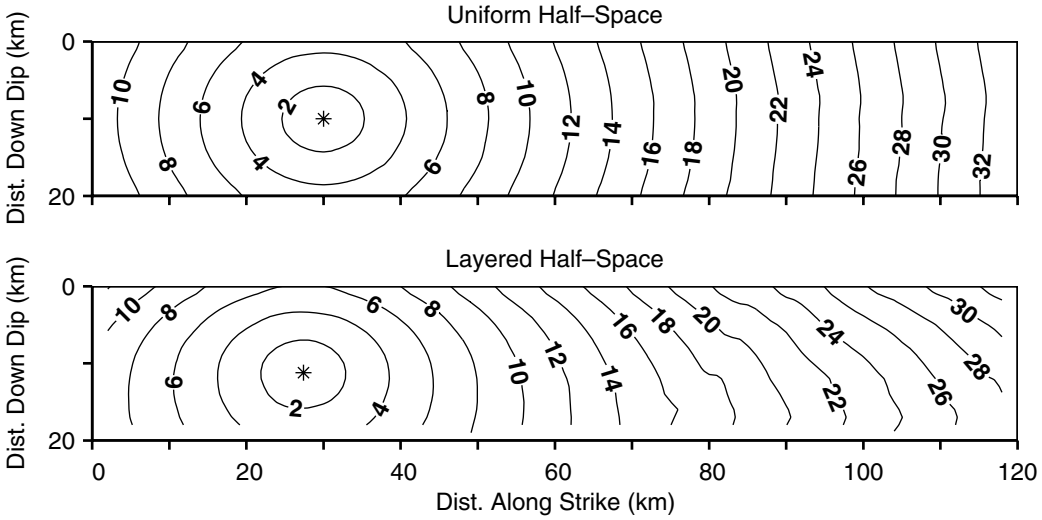


Figure 4. Progression of the leading edge of rupture as shown by contours of slip starting time (in seconds) for the uniform half-space (top) and the layered half-space (bottom) for a rupture propagating at 85% of the local shear-wave speed in the mode-II direction and 20% slower in the mode-III direction. In both cases, the rupture propagates predominantly in the mode-II (horizontal) direction. In the layered half-space the rupture propagates faster at depth and drives the rupture along the surface. The hypocenters indicated by the stars sit 30.0 km and 27.2 km along strike at depths of 10.0 km and 11.2 km, respectively. Roughness in the contours for the layered half-space arise from generating contours from an unstructured finite-element mesh with significant variations in element size.

Table 2
Rupture Speeds in the Mode-II and Mode-III Directions for Each Simulation

| Rupture Speed ($v_s$) | |
|---|---|
| Mode II | Mode III |
| 0.850 | 0.680 |
| 0.925 | 0.740 |
| 1.000 | 0.800 |
| 1.10 | 0.883 |
| 1.21 | 0.966 |
| ($\sqrt{2}$) 1.41 | 1.13 |
| 1.57 | 1.26 |
| ($\sqrt{3}$) 1.73 | 1.39 |
| 2.60 | 2.08 |
| ($2\sqrt{3}$) 3.46 | 2.77 |
| $\infty$ | $\infty$ |

entations with a 2° resolution. For the bandwidth of these simulations ($T > 2$ sec), the maximum peak-to-peak amplitude of a time history resolved into any given direction generally corresponds to the difference between the maximum velocity and minimum velocity. The maximum velocity distributions for rupture propagation at or below the shear-wave speed exhibit the tear-drop shape associated with rupture directivity along the strike of the fault. The maximum peak-to-peak velocities for mode-II rupture at the shear-wave speed are particularly large (approaching 4 m/sec), as one expects for this case of maximum along-strike directivity. As mentioned earlier in the discussion of the snapshots of velocity on the ground surface, the anisotropic rupture speed in the layered medium, as well as the limited bandwidth of the model, prevents the velocities from approaching the theoretical limit of infinite amplitude.

For ruptures propagating between the shear-wave and dilatational-wave speeds (intersonic speeds), the lack of rupture directivity in the along-strike direction greatly diminishes the prominence of the tear-drop shape in the distribution of the maximum amplitudes; peak-to-peak velocities are generally less than 2 m/sec, and they decay less rapidly with distance perpendicular to the fault. As the rupture speed moves into the supersonic range, the displacements and velocities within one fault width (20 km) of the fault increase from about 2 m and 2 m/sec to about 2.5 m and 3 m/sec, respectively, due to the nearly simultaneous rupture. That is, the motions are dominated by a planar shear wave propagating perpendicular to the fault.

In addition to the changes in the spatial distribution of the shaking, we also observe changes in the orientation of the maximum motion, as briefly outlined in our discussion of the snapshots of velocity. Figure 7 shows the orientation of the maximum horizontal displacements and peak-to-peak velocities in the layered half-space. The uniform half-space simulations display the same general trends but exhibit less spatial variation due to the uniform slip. For rupture speeds at or below the shear-wave speed, the maximum peak-to-peak velocities close to the fault exhibit a very strong preference toward a fault-perpendicular orientation (except near

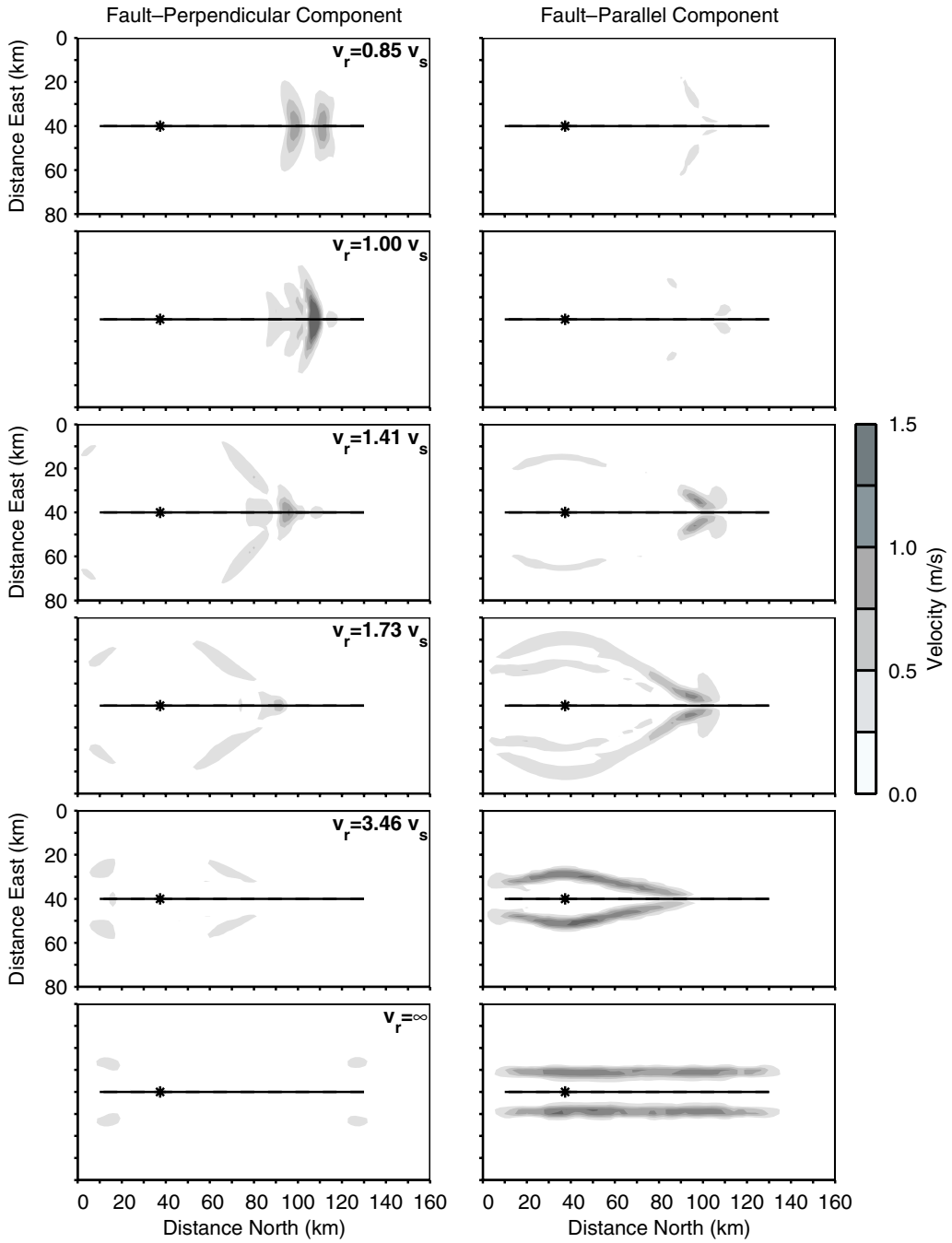


Figure 5. Snapshots of the fault-perpendicular and fault-parallel components of the velocity on the ground surface. The solid line delineates the fault trace, and the asterisk identifies the epicenter. The snapshots for each rupture speed correspond to the time at which the rupture at the surface has propagated approximately 65 km down the fault, except for the case of an infinite rupture speed for which the snapshot is taken at 6.0 sec after the initiation of rupture. As the rupture speed increases, the amplitude of the shear wave radiated along the strike of the fault decreases, whereas the amplitude of the shear wave radiated perpendicular to the fault increases.

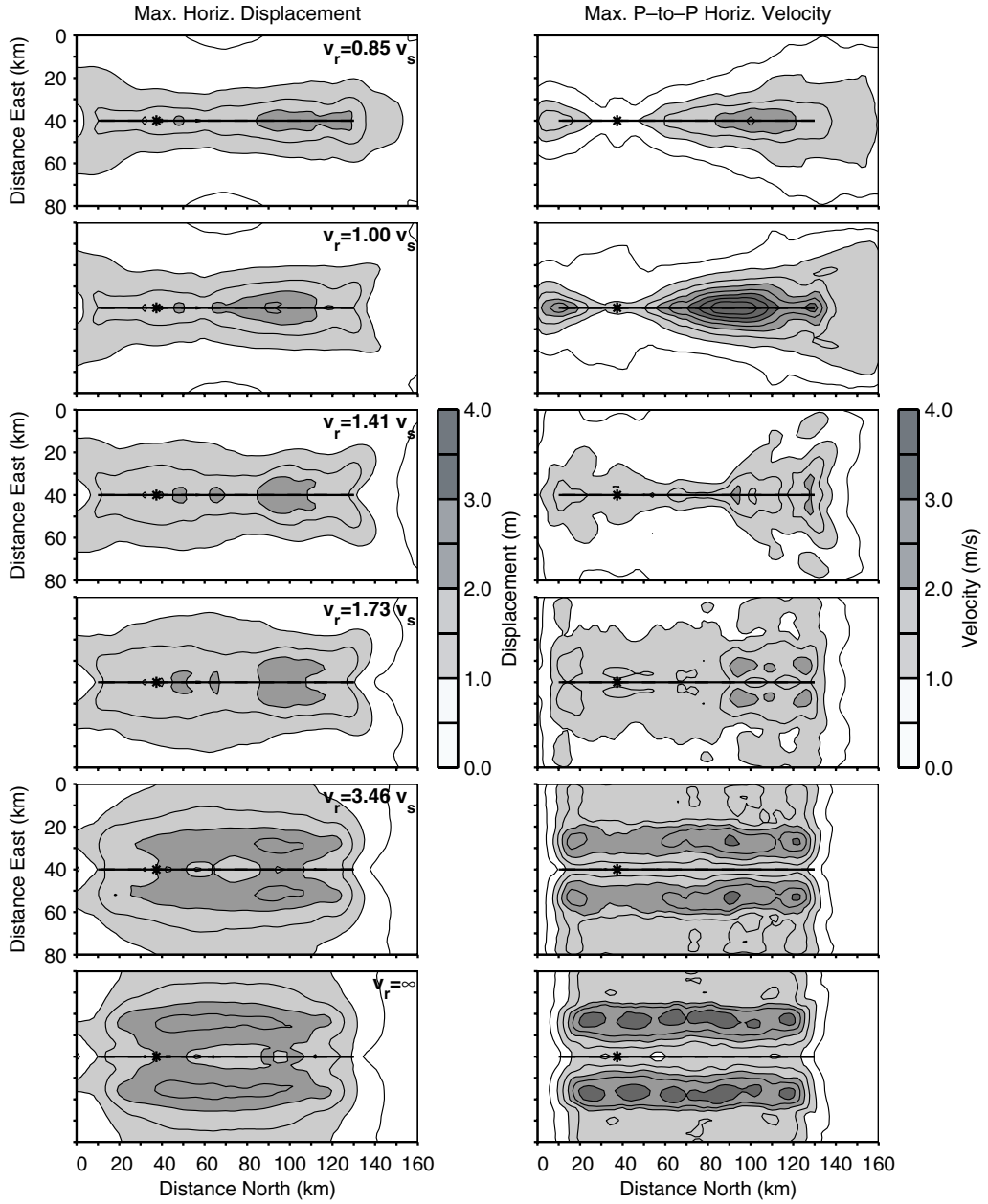


Figure 6. Maximum horizontal displacements and peak-to-peak velocities on the ground surface for six rupture speeds. The solid line delineates the fault trace, and the asterisk identifies the epicenter. Increasing the rupture propagation from subshear speeds to supersonic speeds shifts the distribution of shaking from a tear-drop shape associated with larger amplitudes along the strike of the fault away from the epicenter to an elliptical shape associated with very large amplitudes along the entire strike of the fault at distances out to one fault width from the fault trace.

the epicenter). Increasing the rupture speed into the intersonic range rotates the orientation of the maximum amplitudes toward the fault-parallel direction. For rupture at the Eshelby speed ($\sqrt{2}$ times the shear-wave speed), even though we can identify a gross shift away from a fault-perpendicular orientation, the orientation of the maximum motion is spatially very heterogeneous because of the random distribution of slip. As the rupture speed increases further, the spatial variability in the orientation of the peak motion disappears. When the rupture speed approaches infinity, all locations have similar motions parallel to the strike of the fault; only areas near the ends of the fault have significant fault-perpendicular components.

As discussed earlier, supershear rupture speeds produce large-amplitude fault-parallel motion *before* fault-perpendicular motion at locations close to the fault; this is

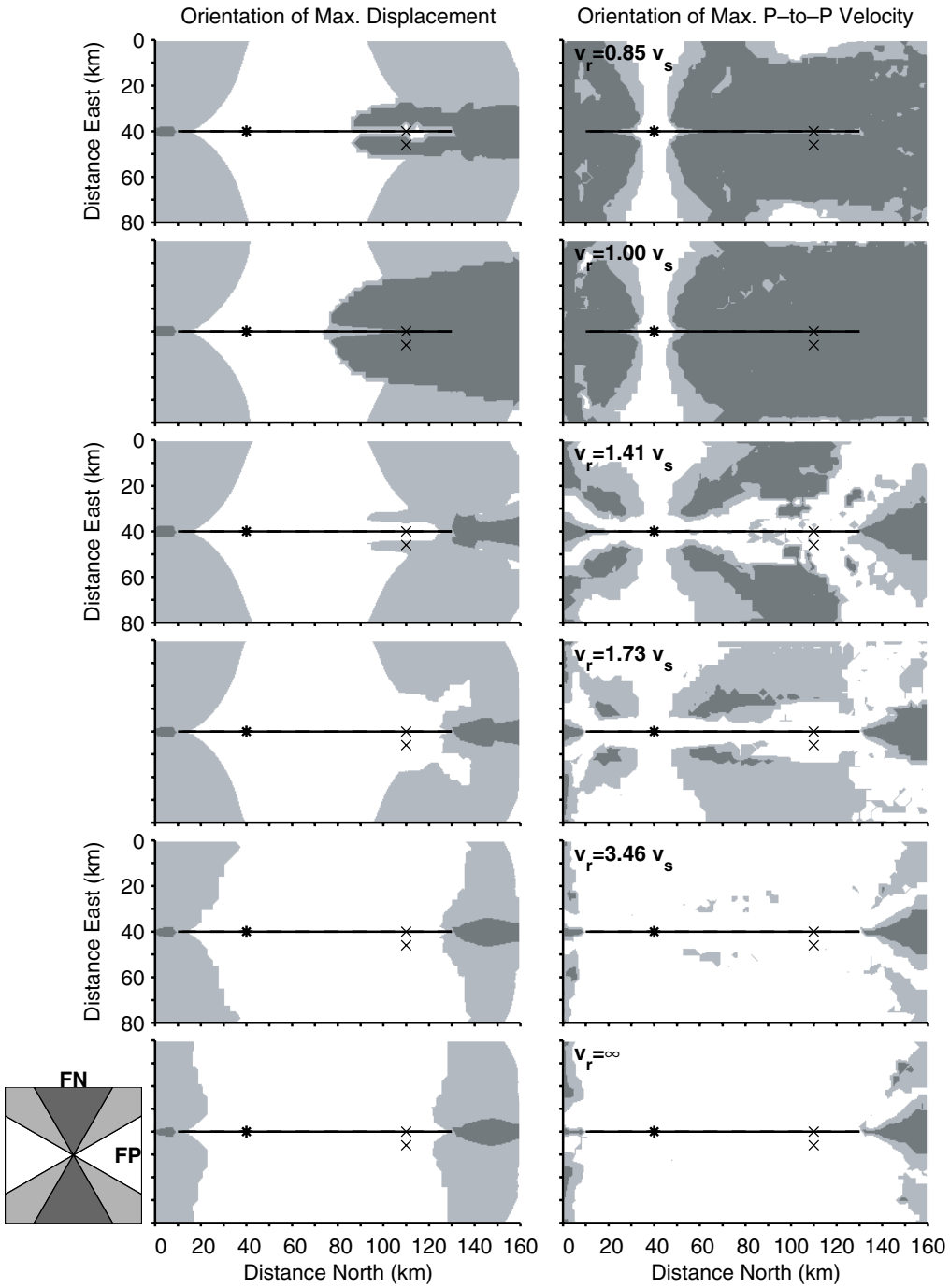


Figure 7. Orientation of the maximum horizontal displacements and peak-to-peak velocities for six rupture speeds. The solid line delineates the fault trace, and the asterisk identifies the epicenter. The maximum motion rotates from predominantly fault-perpendicular (FN) to fault-parallel (FP) orientations as the rupture propagation moves from subshear speeds to supersonic speeds. Figure 8 shows the velocity time histories for the sites designated by ×.

the opposite of what happens at subshear rupture speeds. The polarization of the horizontal motion for two sites located near the northern end of the rupture (Figs. 8 and 9) illustrates this trend. For subshear rupture in both the layered half-space and the uniform half-space, the site along the fault trace experiences large-amplitude fault-perpendicular motion before fault-parallel motion. Rupture at the shear-wave speed accentuates this feature. At both sites, as the rupture speed increases above the shear-wave speed, the fault-parallel motion increases in amplitude and arrives earlier

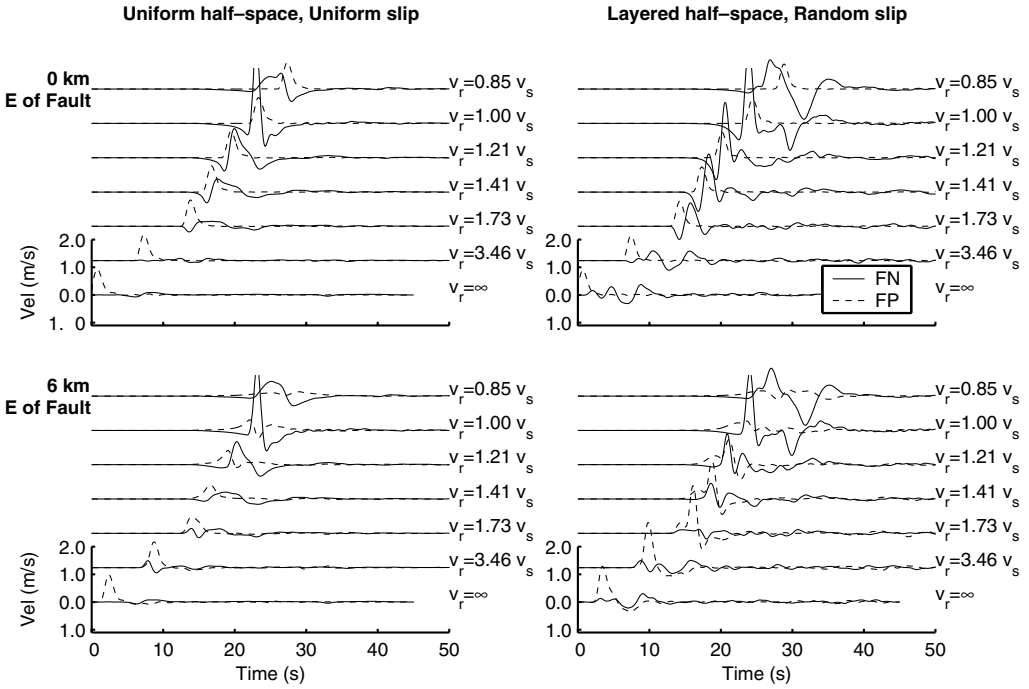


Figure 8. Fault-parallel (FP) and fault-perpendicular (FN) velocity time histories at two sites (see Figs. 1 and 7) for seven different rupture speeds in the uniform half-space with uniform slip (*left*) and the layered half-space with random slip (*right*). The sites lie 0 km or 6 km east of the fault near the north end (100 km along strike). These time histories illustrate that for sites near the rupture, at subshear propagation speeds the energy arrives with strong fault-perpendicular motion. As the rupture speed increases, the energy arrives with increasingly earlier and larger fault-parallel motion, whereas the fault-perpendicular motion decreases.

relative to the fault-perpendicular motion. These features are present at sites all along the fault (except very close to the epicenter). However, this polarization becomes weaker with increasing distance from the rupture because of the decreasing influence of the far-field shear wave with fault-perpendicular motion relative to the other phases. The striking similarity of these trends in the layered half-space and the uniform half-space indicates that they are tied to the effect of the rupture speed on the radiation of the seismic waves at the leading edge of the rupture; they are relatively independent of the details of the geologic structure (layered versus uniform half-space) and spatial variations in slip (low-pass-filtered random slip versus uniform slip).

Figure 10, which displays the overall maximum fault-parallel and fault-perpendicular displacement and peak-to-peak velocity on the ground surface, summarizes this change in polarization of the motion as a function of rupture speed. Because only the largest offsets along the fault trace control the overall maximum fault-parallel displacements, we find very little change in the overall maximum fault-parallel displacements as the rupture speed increases to intersonic and supersonic speeds. This explains why the uniform half-space with uniform slip has a much smaller maximum fault-parallel displacement than the layered half-space with random slip. The fault-perpendicular displacements, on the other hand, are sensitive to the amount of rupture directivity induced reinforcement of the far-field shear wave radiated along the strike of the fault, so that the overall maximum displacement is largest for rupture speeds near the shear-wave speed. The overall maximum fault-perpendicular peak-to-peak velocity displays a similar trend; the overall maximum peak-to-peak fault parallel component increases with rupture speed, following the rotation of maximum motion from fault perpendicular to fault parallel directions.

While the distribution of slip and slip rate are identical in all of the simulations, the profound differences in directivity mean that the radiated energy varies with rupture speed (Haskell, 1964). Figure 11 shows how rupture speed affects the energy dissipated at the absorbing boundaries on the truncated edges of the domain (radiated energy). By continuing the simulation until there is negligible kinetic energy left in the domain, the boundaries absorb all of the energy radiated into the far-field. In the layered half-space, the depth variation of the rupture speed resulting from the depth-dependent structure reduces the amount of directivity. As a result, the local maximum in the radiated energy near the shear-wave speed is smaller for the layered half-space than for the uniform half-space.

The radiated energy reaches a local minimum at the Eshelby speed ($\sqrt{2}$ times the shear-wave speed). This is con-

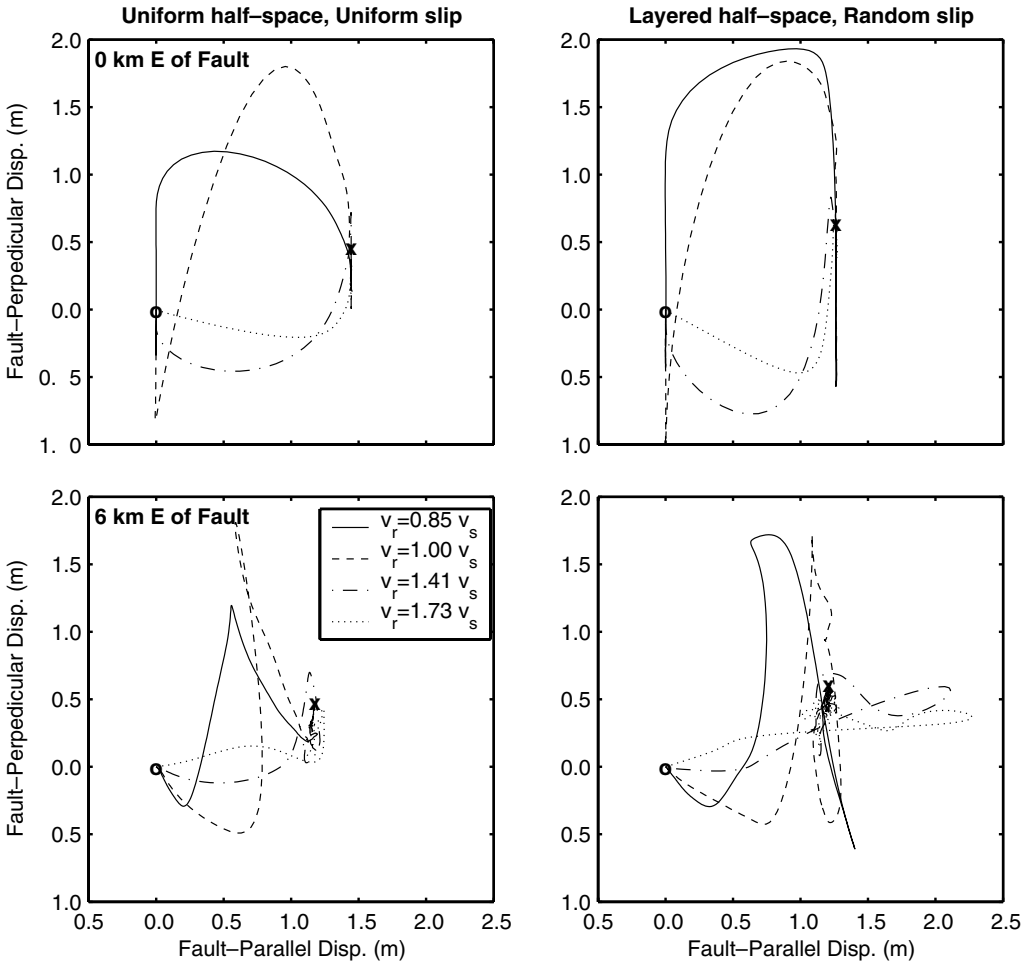


Figure 9. Displacement trajectories at two sites (same sites as in Fig. 8) for four different rupture speeds in the uniform half-space with uniform slip (left) and the layered half-space with random slip (right). The trajectories begin at the origin (denoted by circles) and end at the Xs. The trajectories demonstrate that sites very close to the fault experience fault-parallel motion *after* fault-perpendicular motion for subshear rupture, whereas for supershear rupture, the sites experience fault-parallel motion *before* significant fault-perpendicular motion. Beginning at distances of around 6 km from the fault, the effects of the dilatational wave become significant, and this feature disappears.

sistent with stable propagation of dynamic shear cracks at this rupture speed with "subsonic-like" behavior (Freund, 1979). The sharp arrival of the shear wave associated with the Mach cone generates large velocities so that the energy radiated by intersonic ruptures exceeds the energy radiated by ruptures propagating below the shear-wave speed. As the rupture speed increases to infinity, the radiated energy gradually increases to its asymptotic limit; when the rupture speed is infinite, most of the energy is in the far-field shear wave, propagating as a plane wave perpendicular to the simultaneous rupture.

## Discussion

This set of simulations illustrates that as the sustained rupture speed increases from below the shear-wave speed to near the dilatational-wave speed, three changes take place: (1) at locations within a few kilometers of the surface rupture, the shear wave with fault-parallel particle motion arrives before, rather than after, the shear wave with fault-perpendicular motion; (2) rupture directivity along the strike of the fault is lost, so that the maximum horizontal peak-to-peak velocities no longer increase along the strike of the fault away from the epicenter, and they decay less rapidly with distance from the fault; and (3) the orientations of the maximum peak-to-peak velocities rotate from being predominantly fault-perpendicular to being predominantly fault-parallel.

As mentioned earlier, these simulations use a uniform mode-II rupture speed, whereas the rupture speed in real earthquakes fluctuates and may be supershear over only part of the rupture. Can the three diagnostics for supershear rup-

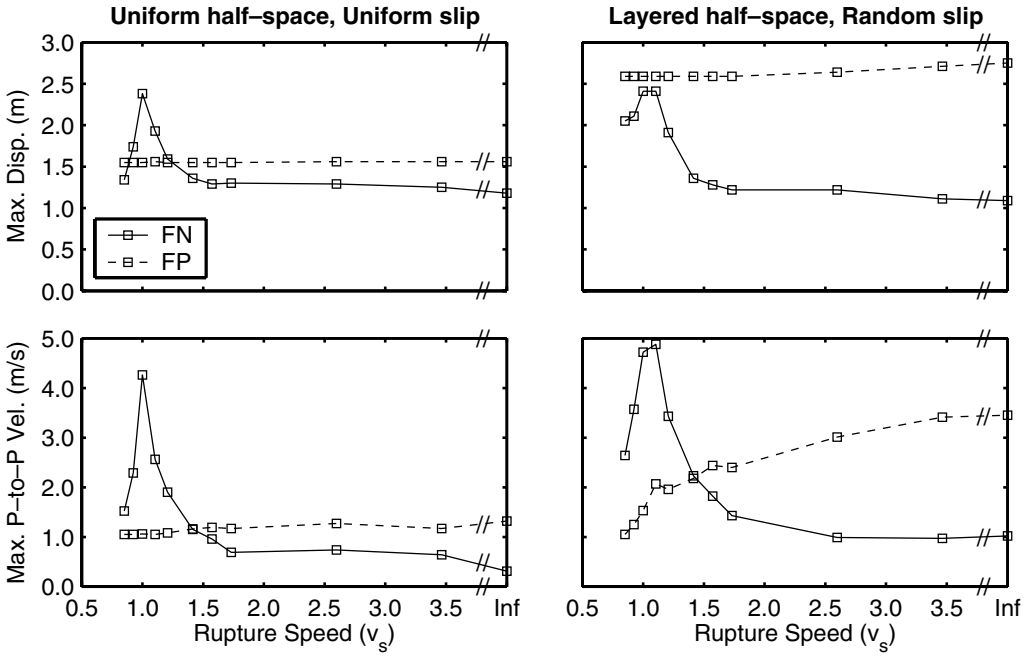


Figure 10. Overall maximum fault-parallel (FP) and fault-perpendicular (FN) displacement and peak-to-peak velocity for any point on the ground surface as a function of rupture speed. The left column shows the values for the uniform half-space with uniform slip, and the right column shows the values for the layered half-space with random slip. The maximum motions rotate from predominantly fault perpendicular to fault parallel as the rupture speed increases to intersonic and supersonic speeds. The two models display very similar behavior, although the random spatial variation in slip in the layered half-space results in a much larger maximum fault-parallel displacement.

ture help to interpret records from suspected cases of supershear rupture in real earthquakes? It might be possible to infer supershear rupture if the maximum ground velocities are nearly fault-parallel for stations close to the fault. Of course, this requires that the energy arriving at the site (which is related to the velocity amplitude) from the supershear portion of the rupture exceeds that arriving from the subshear portion of the rupture. If only a small portion of the rupture jumps to supershear speeds (regardless of how close this occurs to the recording site), this condition will likely not be met. In such cases, the near-source ground motions may be relatively unaffected by supershear rupture. Thus, the presence of slip heterogeneity means that it would be difficult to argue for supershear rupture based on the orientation of peak ground motions at only a few stations. On the other hand, the ground-motion time histories recorded close to the portion of the fault where the rupture may have propagated faster than the shear wave could be affected and may exhibit significant fault-parallel motion prior to fault-perpendicular motion.

The 1999 Izmit, Turkey, earthquake has been simulated with supershear rupture. Unfortunately, there was only one near-source station (Sakarya, SKR) along the fault trace in the direction of the suspected supershear rupture (east of the epicenter), and it failed to accurately record the north–south (fault-perpendicular) motion. Consequently, we cannot examine the orientation of the maximum velocity or the polarization of the shear-wave motion at this station in order to look for evidence of supershear rupture. However, in two other cases of strike-slip events with suspected supershear rupture, the 1979 Imperial Valley, California, and the 2002 Denali fault, Alaska, earthquakes, ground motions were recorded within a few kilometers of the fault trace near the areas with suspected supershear rupture.

In the Imperial Valley earthquake, five stations within a few kilometers of the fault (Fig. 12) recorded the ground motions. The portion of the fault between station EMO and the strong-motion array contains the portion of the rupture suspected of propagating faster than the shear-wave speed. We apply $v_0$ baseline corrections (Boore, 2001) to the uncorrected acceleration time histories (Porcella *et al.*, 1982; Porter, 1982) before integrating to obtain velocity time histories. The records are then low-pass filtered using a fourth-order (four poles, causal) Butterworth filter with the passband extending to 0.5 Hz. Because the velocity records contain numerous oscillations even after low-pass filtering, the maximum peak-to-peak velocity measured using consecutive peaks is considerably smaller than the peak velocity, so to find the orientation of the maximum motion we use the peak velocity as opposed to the peak-to-peak velocity (which we used in the earlier discussion and has a similar orientation for the simulations). The maximum velocities at

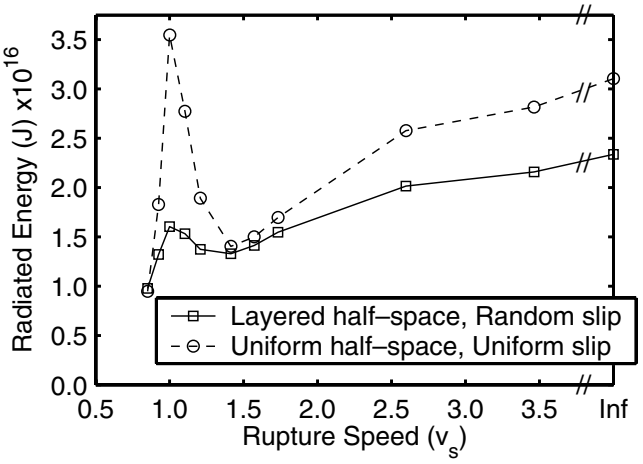


Figure 11. Far-field radiated energy as a function of rupture speed for both the uniform half-space with uniform slip and the layered half-space with random slip. The maximum in the shear-wave radiation pattern along the strike of the fault results in a significant increase in the radiated energy for rupture speeds approaching the shear-wave speed. In the layered half-space, the depth variation in the shear-wave speed limits the amplitude of the peak in radiated energy for a rupture propagating at the shear-wave speed. The local minimum for intersonic rupture occurs at the Eshelby speed. Approaching supersonic speeds, the radiated energy increases because of effective reinforcement of the shear waves radiated perpendicular to the fault.

all five stations are closely aligned to the fault-perpendicular direction. This suggests that most of the energy arriving at the stations corresponds to a rupture propagating near the shear-wave speed.

The velocity waveforms support subshear rupture propagation. Stations EMO, E06, and E07 all experience large-amplitude fault-perpendicular motion that arrives prior to the largest fault-parallel motion, consistent with subshear rupture as illustrated by the close correspondence to seismograms from similar locations in the simulations with ruptures propagating at or below the shear-wave speed. Note that all of the simulations use a uniform mode-II rupture speed. Stations E05 and E08 do not fit the subshear pattern as well, but they are more distant from the fault; station E05 may also be affected by the nearby branching of the rupture. Thus, we find the orientation of the motion and the waveforms are consistent with most of the energy being generated by subshear rupture. This generally agrees with the observations of predominantly subshear rupture in more detailed studies (Olson and Apsel, 1982; Hartzell and Heaton, 1983; Archuleta, 1984; Spudich and Cranswick, 1984). Unfortunately, the results presented here do not help resolve the issue of whether a limited portion of the rupture (approximately 10 km in length) propagated faster than the shear-wave speed.

Archuleta (1984) argued that the region of supershear rupture may be too far to the south for detection with observations of the polarization of the motion using the El Centro strong-motion array. Spudich and Cranswick (1984) investigated the apparent velocity of high-frequency dilatational-wave phases recorded on the El Centro differential array. They found that these apparent velocities were consistent with a small patch of supershear rupture, although that interpretation may not be unique. Unfortunately, the diagnostics we develop here are not appropriate for detecting such localized patches of supershear rupture.

In the 2002 Denali fault earthquake the ground motion was recorded within a few kilometers of the fault along the Alyeska pipeline at pump station 10. This location sits about 65 km along the fault from where the strike-slip rupture began. We again low-pass filter the velocity record using a fourth-order Butterworth filter to match the bandwidth of the simulations ($T > 2$ sec). To compare the velocity record from pump station 10 to our suite of strike-slip simulations with uniform rupture speeds, we place the simulation epicenter at the junction of the Susitna Glacier and Denali faults (where the rupture transitioned from oblique slip on the Susitna Glacier fault to predominantly lateral slip on the Denali fault). An 8-sec delay applied to the pump station 10 time histories accounts for the dilatational-wave travel time from the hypocenter ($+15$ sec) (Ellsworth *et al.*, 2004), delayed rupture on the the Denali fault ($-9$ sec) [Chen Ji, 2003], and differences in the nominal shear-wave speed in Alaska (Ellsworth *et al.*, 2004) compared to the simulations ($+2$ sec).

The timing of the shear-wave arrival would be consistent with an average rupture speed from the Susitna Glacier fault to pump station 10 at 80% of the shear-wave speed. On the other hand, the velocity waveforms suggest that the energy arriving at pump station 10 may have been generated by locally supershear rupture. Figure 13 shows that the orientation of the peak velocity lies closer to the fault-parallel direction than the fault-perpendicular direction (consistent with our simulations of supershear rupture). Furthermore, the first large-velocity pulse on the fault-parallel component has an amplitude at least as large as the fault-perpendicular component (using either the average fault orientation or the local fault orientation). Examining the velocity time histories from the corresponding location in the simulations for the various rupture speeds, we find a mode-II rupture speed between 10% and 20% above the shear-wave speed provides the best overall qualitative fit. The relative amplitudes of the fault-parallel and fault perpendicular components are more closely fit by mode-II rupture speeds 20%–40% above the shear-wave speed, but the nearly simultaneous arrival of the two components is more closely fit by rupture speeds closer to the shear-wave speed.

A kinematic source inversion (Chen Ji, 2003) indicates that the average rupture speed remains subshear but allows a short duration of supershear rupture near this location, with shorter durations allowing faster rupture speeds. Detailed modeling by Ellsworth *et al.* (2004) and Dunham and Ar-

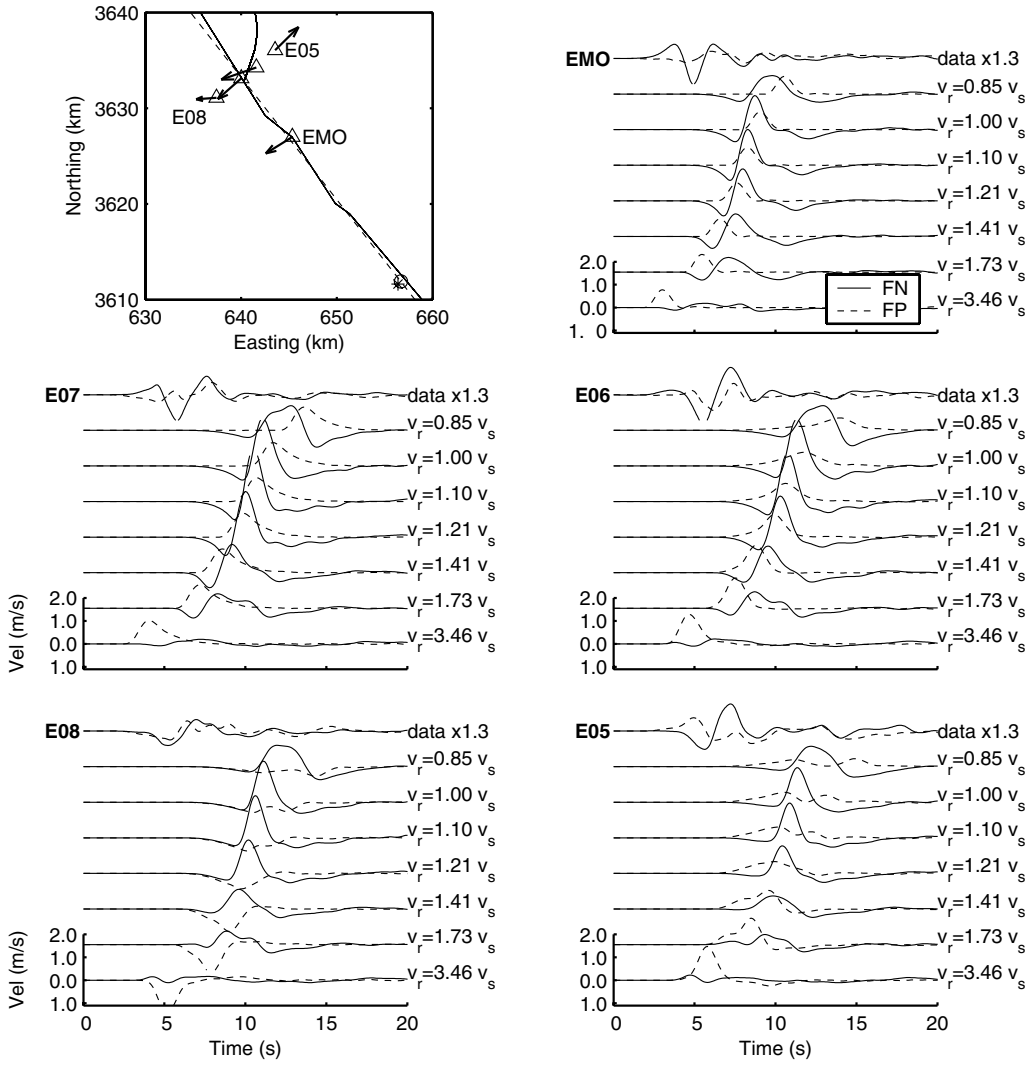


Figure 12. Orientation of the peak velocity (upper left) and comparison of velocity waveforms from the 1979 Imperial Valley earthquake for four stations in the El Centro strong-motion array (stations E05 to E08) and station EMO. The triangles identify the station locations, and the vectors show the amplitude and orientation of the maximum velocity. The solid line indicates the fault trace, and the asterisk identifies the epicenter. The dashed line and open circle show the comparable geometry for the simulations. The maximum velocities are generally aligned with the fault-perpendicular direction, and the stations generally experience significant fault-perpendicular (FN) motion prior to fault-parallel (FP) motion, implying most of the energy was generated while the rupture propagated slower than the shear-wave speed.

chuleta (2004) suggests the rupture speed may have exceeded the shear-wave speed by up to 50%–60% over a distance of about 15 km just west of pump station 10. Thus, the orientation of the maximum velocity and the polarization of motion appears consistent with supershear rupture immediately to the west of pump station 10 in the Denali fault earthquake and agrees with the much more in-depth analysis by Ellsworth *et al.* (2004) and dynamic rupture modeling of Dunham and Archuleta (2004). In this case, the supershear rupture appears to have been of sufficient duration and to have occurred close enough to the recording station for the recorded motion to exhibit the characteristics of supershear rupture found in our simulations.

## Conclusions

We simulated kinematic ruptures of $M$ 7.4 events on a strike-slip fault with different rupture speeds, including ruptures that propagate below the shear-wave speed (subsonic), between the shear-wave speed and the dilatational wave-speed (intersonic), or above the dilatational wave-speed (supersonic). Increasing the rupture speed to values faster than

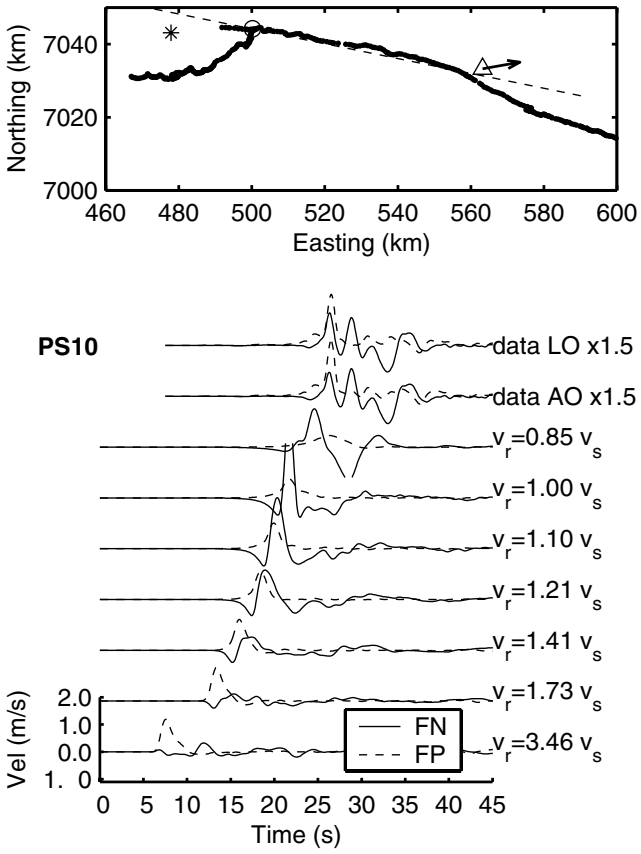


Figure 13. Orientation of the peak velocity (top) and comparison of velocity waveforms from the 2002 Denali fault earthquake for the pump station 10 record. The triangles identify the station location, and the vector shows the amplitude and orientation of the maximum velocity. The thick solid line indicates the fault trace, and the asterisk identifies the epicenter. The dashed line and open circle show the comparable geometry for the simulations. The data are shown with fault-parallel (FP) and fault-perpendicular (FN) components relative to the local fault orientation (LO) and the average fault orientation (AO). An 8-sec time delay applied to the data to allows a more direct comparison with the simulations. The orientation of the peak velocity and the velocity waveforms fit the pattern for rupture above the shear-wave speed.

the shear-wave speed reduces the rupture directivity induced reinforcement of the far-field shear waves propagating down the fault, resulting in smaller-amplitude directivity pulses. As the rupture speed is increased through the intersonic range, the rupture begins to more effectively reinforce shear waves radiated perpendicular to the fault. As a result, the maximum velocities remain relatively uniform along the strike of the fault, but the displacements and velocities decay less rapidly with distance perpendicular to the fault. Additionally, the orientation of the maximum horizontal displacements and peak-to-peak velocities rotate from predominantly fault-perpendicular to predominantly fault-parallel directions in regions close to the fault. However, these changes may be difficult to observe if there are a limited number of observations; heterogeneity in the distribution of slip creates fluctuations in the orientation of the peak motion. A more robust characteristic for supershear rupture is the arrival of fault-parallel motion prior to fault-perpendicular motion at sites very close to the rupture. This was evident from its clear display in the simulations of both a layered half-space with random slip and a uniform half-space with uniform slip.

Based on these simulation results, we examined long-period near-source recordings from the 1979 Imperial Valley and 2002 Denali fault earthquakes, in which others have found some evidence for supershear rupture. In the Imperial Valley earthquake, the long-period ground motions contain much more energy in the fault-perpendicular direction compared with the fault-parallel direction, suggesting predominantly subshear rupture. This is consistent with previous studies that found the rupture remained below the shear-wave speed or only a limited portion of the rupture exceeded the shear-wave speed. The polarization of the velocity waveforms are also consistent with subshear rupture, suggesting supershear rupture, if it occurred, was limited to a small portion of the fault away from the locations that recorded the ground motion very close to the fault rupture. On the other hand, in the 2002 Denali fault earthquake, the recording closest to the fault exhibits characteristics found in the simulations with rupture above the shear-wave speed: orientation of the peak velocity away from fault-perpendicular direction and nearly simultaneous arrival of large-amplitude motion in the fault-perpendicular and fault-parallel directions. Thus, these simulations and recordings provide additional support for the existence of supershear ruptures in earthquakes but illustrate the difficulty in obtaining definitive evidence without a dense seismic network along the surface trace of the fault.

## Acknowledgments

We thank Ralph Archuleta, Paul Spudich, David Wald, and an anonymous reviewer for their constructive comments, which improved the manuscript. Access to the Hewlett-Packard V-Class computer was provided by California Institute of Technology's Center for Advanced Computing Research through the National Partnership for Advanced Computational Infrastructure—A Distributed Laboratory for Computational Science and Engineering, supported by the NSF cooperative agreement ACI-9619020.

## References

Aagaard, B. T., T. H. Heaton, and J. F. Hall (2001). Dynamic earthquake ruptures in the presence of lithostatic normal stresses: implications for friction models and heat production, *Bull. Seis. Soc. Am.* **91,** 1765–1796.

Aagaard, B. T., J. F. Hall, and T. H. Heaton (2004). Effects of fault dip and slip rake angles on near-source ground motions: why rupture directivity was minimal in the 1999 Chi-Chi, Taiwan, earthquake, *Bull. Seism. Soc. Am.* **94,** 155–170.

Anderson, J. G. (2000). Implications for seismic hazard analysis, in *Kocaeli, Turkey, Earthquake of August 17, 1999: Reconnaissance Re-*

*port*, Vol. 16, Earthquake Engineering Research Institute, Oakland, California, 113–137.

Andrews, D. J. (1976). Rupture velocity of plane strain shear cracks, *J. Geophys. Res.* **81,** 5679–5687.

Archuleta, R. J. (1984). A faulting model for the 1979 Imperial Valley earthquake, *J. Geophys. Res. Solid Earth* **89,** 4559–4585.

Boore, D. M. (2001). Effect of baseline corrections on displacements and response spectra for several recordings of the 1999 Chi-Chi, Taiwan, earthquake, *Bull. Seism. Soc. Am.* **91,** 1199–1211.

Bouchon, M., and M. Vallee (2003). Observation of long supershear rupture during the magnitude 8.1 Kunlunshan earthquake, *Science* **301,** 824–826.

Bouchon, M., N. Toksoz, H. Karabulut, M. P. Bouin, M. Dietrich, M. Aktar, and M. Edie (2000). Seismic imaging of the 1999 Izmit (Turkey) rupture inferred from the near-fault recordings, *Geophys. Res. Lett.* **27,** 3013–3016.

Bouchon, M., M. P. Bouin, H. Karabulut, M. N. Toksoz, M. Dietrich, and A. J. Rosakis (2001). How fast is rupture during an earthquake? New insights from the 1999 Turkey earthquakes. *Geophys. Res. Lett.* **28,** 2723–2726.

Broberg, K. B. (1994). Intersonic bilateral slip, *Geophys. J. Int.* **119,** 706–714.

Broberg, K. B. (1995). Intersonic mode II crack expansion, *Arch. Mech.* **47,** 859–871.

Burridge, R. (1973). Admissible speeds for plane-strain self-similar shear cracks with friction but lacking cohesion, *Geophys. J. R. Astr. Soc.* **35,** 439–455.

Das, S. (1981). Three-dimensional spontaneous rupture propagation and implications for the earthquake source mechanism, *Geophys. J. R. Astr. Soc.* **67,** 375–393.

Das, S., and K. Aki (1977). A numerical study of two-dimensional spontaneous rupture propagation, *Geophys. J. R. Astr. Soc.* **50,** 643–668.

Day, S. M. (1982). Three-dimensional simulation of spontaneous rupture: the effect of nonuniform prestress, *Bull. Seism. Soc. Am.* **72,** 1881–1902.

Dunham, E. M., and R. J. Archuleta (2004). Evidence for a supershear transient during the 2002 Denali earthquake, *Bull. Seism. Soc. Am.* (in press).

Ellsworth, W. L., M. Celebi, J. R. Evans, E. G. Jensen, M. C. Metz, D. J. Nyman, J.W. Roddick, P. Spudich, and C. D. Stephens (2004). Near-field ground motions of the *M* 7.9 November 3, 2002, Denali fault, Alaska, earthquake recorded at pump station 10, *Earthquake Spectra* **20,** 597–615.

Freund, L. B. (1979). The mechanics of dynamic shear crack propagation, *J. Geophys. Res. Solid Earth* **84,** 2199–2209.

Freund, L. B. (1990). *Dynamic Fracture Mechanics*. Cambridge monographs on mechanics and applied mathematics. Cambridge University Press, New York.

Hartzell, S. H., and T. H. Heaton (1983). Inversion of strong ground motion and teleseismic waveform data for the fault rupture history of the 1979 Imperial Valley, California, earthquake, *Bull. Seism. Soc. Am.* **73,** 1553–1583.

Haskell, N. (1964). Total energy and energy spectral density of elastic wave propagation from propagating faults, *Bull. Seism. Soc. Am.* **54,** 1811–1841.

Heaton, T. H. (1990). Evidence for and implications of self-healing pulses of slip in earthquake rupture, *Phys. Earth Planet. Interiors* **64,** 1–20.

Madariaga, R., and K. B. Olsen (2000). Criticality of rupture dynamics in 3-D, *Pure Appl. Geophys.* **157,** 1981–2001.

Madariaga, R., K. Olsen, and R. Archuleta (1998). Modeling dynamic rupture in a 3D, earthquake fault model, *Bull. Seism. Soc. Am.* **88,** 1182–1197.

Olson, A. H., and R. J. Apsel (1982). Finite faults and inverse-theory with applications to the 1979 Imperial Valley earthquake, *Bull. Seism. Soc. Am.* **72,** 1969–2001.

Porcella, R. L., R. B. Matthiesen, and R. P. Maley (1982). Strong-motion data recorded in the United States, in *The Imperial Valley, California, Earthquake of October 15, 1979*, pp. 289–318. USGS Prof. Paper 1254.

Porter, L. D. (1982). Data-processing procedures for main-shock motions recorded by the California Division of Mines and Geology strong-motion network, in *The Imperial Valley, California, Earthquake of October 15, 1979, U.S. Geol. Surv. Profess. Pap. 1254*, 407–432.

Rosakis, A. J., O. Samudrala, and D. Coker (1999). Cracks faster than the shear-wave speed, *Science* **284,** 1337–1340.

Samudrala, O., Y. Huang, and A. J. Rosakis (2002). Subsonic and intersonic shear rupture of weak planes with a velocity weakening cohesive zone. *J. Geophys. Res. Solid Earth* **107,** no. B8, 2170. doi 10.1029/2001JB000460.

Sekiguchi, H., and T. Iwata (2002). Rupture process of the 1999 Kocaeli, Turkey, earthquake estimated from strong-motion waveforms, *Bull. Seism. Soc. Am.* **92,** 300–311.

Somerville, P. G., N. F. Smith, R. W. Graves, and N. A. Abrahamson (1997). Modification of empirical strong ground motion attenuation relations to include the amplitude and duration effects of rupture directivity, *Seism. Res. Lett.* **68,** 199–222.

Spudich, P., and E. Cranswick (1984). Direct observation of rupture propagation during the 1979 Imperial Valley earthquake using a short baseline accelerometer array, *Bull. Seism. Soc. Am.* **74,** 2083–2114.

Thio, H. K., R. W. Graves, J. Polet, T. Sato, T. Ishii, and P. G. Somerville (2004). The rupture process of the 1999 Kocaeli (Turkey) earthquake, *J. Geophys. Res. Solid Earth* (in press).

Xia, K., A. J. Rosakis, and H. Kanamori (2004). Laboratory experiments: the sub-Rayleigh-to-supershear rupture transition, *Science* **303,** 1859–1861.

U.S. Geological Survey, MS977
345 Middlefield Rd.
Menlo Park, California 94025
(B.T.A.)

Department of Geologic and Planetary Sciences
Mail Stop 252-21
California Institute of Technology
Pasadena, California 91125
(T.H.H.)

Manuscript received 22 December 2003.